Cytotoxic BODIPY-Appended Half-Sandwich Iridium(III) Complex Forms Protein Adducts and Induces ER Stress

Robin Ramos, Jean-François Gilles, Romain Morichon, Cédric Przybylski,
Benoît Caron, Candice Botuha, Anthi Karaiskou, Michèle Salmain, Joëlle
Sobczak-Thépot

A cytotoxic BODIPY-appended half-sandwich iridium(III) complex forms protein adducts and induces ER stress

Robin Ramos,†‡ Jean-François Gilles,# Romain Morichon,‡ Cédric Przybylski†, Benoît Caron,§ Candice Botuha,† Anthi Karaiskou,‡ Michèle Salmain*† and Joëlle Sobczak-Thépot*‡

† Institut Parisien de Chimie Moléculaire (IPCM), Sorbonne Université, CNRS, 4 place Jussieu, F-75005 Paris, France.
‡ Centre de Recherche Saint Antoine (CRSA), Sorbonne Université, INSERM, 184 rue du Faubourg Saint Antoine, F-75012 Paris, France.
# Imaging Core Facility, CNRS-FR3631-Institut de Biologie Paris Seine, Sorbonne Université, F-75005, Paris, France
§ Sorbonne Université, ISTeP, ALIPP6, 4 place Jussieu 75005 Paris

ABSTRACT: Half-sandwich complexes of iridium(III) are currently being developed as anticancer drug candidates. In this context, we introduce **IrBDP** for which the C^N chelating phenyloxazoline ligand carries a fluorescent and lipophilic BODIPY reporter group, designed for intracellular tracking and hydrophobic compartments tropism. High resolution analysis of cells cultured with **IrBDP** showed that it quickly permeates the plasma membrane, accumulates in mitochondria and the endoplasmic reticulum (ER), generating ER-stress, dispersal of the Golgi apparatus, cell proliferation arrest and apoptotic cell death. Moreover, **IrBDP** forms fluorescent adducts with a subset of amino acids, namely histidine and cysteine, via coordination of N or S donor atoms of their side chain. Consistently, *in vivo* formation of covalent adducts with specific proteins is demonstrated, providing a molecular basis for the observed cytotoxicity and cellular response. Collectively, these results provide a new entry to the development of half-sandwich iridium-based anticancer drugs.

INTRODUCTION

Organometallic iridium(III) complexes have recently attracted attention as anticancer drug candidates and possible alternatives to cisplatin and its congeners oxaliplatin and carboplatin.[1] Two families of iridium(III) complexes can be roughly distinguished, on the one hand the so-called bis-cyclometalated complexes with an octahedral geometry and luminescence properties[2] and on the other hand, the half-sandwich or piano stool complexes with a pseudo-tetrahedral geometry. The latter series comprises an arene ligand (typically a pentasubstituted cyclopentadienyl ligand), a chelating bidentate ligand, the coordination sphere being completed with a monodentate ligand.[3] This ligand is usually labile, hence exchangeable by water following an aquation reaction or by other coordinating species like organosulfur compounds.[4] These complexes can be neutral or cationic according to the charge of the chelating and labile ligands. Generally, they are devoid of luminescence properties except for a few of them, albeit with low quantum yields.[5]

From the already available information on half-sandwich iridium complexes, it appears that their cytotoxic activity depends on the nature of the ligands but the relationship between structure and activity is still rather dim at this point. Some of them were shown to induce the overproduction of reactive oxygen species (ROS) via NAD(P)H catalytic oxidation[6,7] or by ligand-centered redox activation,[8] leading to the onset of an antioxidant response.[9] Nevertheless, it is highly likely that other mechanisms could be at stake to explain their anticancer properties.

One proven strategy to get insight into the mechanism of action of non-luminescent drugs is to append a fluorescent reporter group so as to track them within cells and eventually determine their subcellular distribution[10–12] assuming that the activity is related to the localization. To this end, rhodamine B and G entities have been appended to the chelating ligand of half-sandwich cationic or neutral iridium complexes.[13–15] However, the interpretation of microscopy images of cells treated by rhodamine-labeled complexes can be confusing owing to the known pH and metallic cations dependence of rhodamine derivatives fluorescence emission that may introduce a strong bias in the subcellular localization determination.[16]

An original alternative strategy consists in deliberately addressing the metal complex to specific subcellular compartments by appending a suitable targeting group and determine how the cellular response is consequently affected. A BODIPY moiety could fulfil this function as its lipophilicity generally results in intracellular membranes and lipid droplets accumulation,[17] its photoluminescence properties[18] being an additional asset. BODIPY derivatives are bright, highly photostable fluorophores whose emission properties are generally insensitive to pH changes or polarity, unless specifically designed to do so.[19] BODIPY entities have already been incorporated into various ruthenium(II), gold(I), platinum(II) and iridium(III) complexes (Figure 1) for cell imaging purposes.[20–23] This strategy has also been recently employed to identify the protein binding partners of cisplatin by combining 2D electrophoresis and mass spectrometry.[24]

As part of our research program on the design of iridium-based complexes as potential anticancer drugs, we recently introduced a library of 10 complexes including variously substituted phenyloxazoline derivatives as C^N chelating ligands and showed that their cytotoxicity on HeLa cells was at least partly linked to their ability to raise the level of intracellular H_2O_2.[7] As a continuation to this study, we herein introduce an iridium complex comprising a phenyloxazoline ligand to which was appended a BODIPY entity on the phenyl ring later denominated as **IrBDP**. This position was chosen owing to the stability of the C^N chelating ligand towards decoordination that should allow us to track the iridium complex all the way to its biological targets.
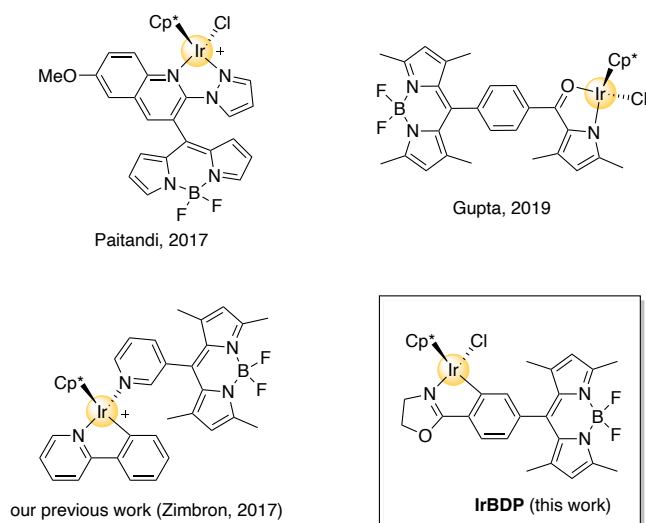
Figure 1. Selected mononuclear half-sandwich iridium(III) complexes comprising a BODIPY moiety for biological applications.

The synthesis, chemical reactivity and photophysical properties of **IrBDP** are presented as well as cell viability and uptake studies in two *in vitro* cell models. Next, the intracellular localization and fate of **IrBDP** is determined by confocal microscopy using fluorescent organelle trackers. Finally, the reactivity of **IrBDP** first with model amino acids then with cellular proteins *in vitro* and *in vivo* is investigated. Altogether this paper aims at providing a comprehensive interpretation of the intracellular localization of this fluorophore-appended complex along with its biological effects and cytotoxicity.

RESULTS AND DISCUSSION

Synthesis and photophysical properties of IrBDP. A phenyloxazoline derivative carrying a BODIPY entity at the 4-position of the phenyl ring (**phox-BDP**) was synthesized in 5 steps. **phox-BDP** exhibited the expected photophysical properties of meso-substituted aryl-BODIPY as summarized in Table S2. Further reaction of **phox-BDP** with $[IrCp^*Cl_2]_2$ in the presence of excess CH_3COONa afforded **IrBDP** in 76% yield as a red solid (synthetic pathway schematized in Figure S1). The structure of **IrBDP** was confirmed by ^1H, ^{13}C NMR spectroscopy and high-resolution mass spectrometry. The oxazoline's hydrogens as well as the methyl groups of the BODIPY scaffold were magnetically inequivalent owing to the chiral environment around the iridium atom.

As expected, **IrBDP** exhibits intense absorption in the visible range with a maximum at ca. 500 nm in most organic solvents and water, due to the 0-0 $S_0 \rightarrow S_1$ transition typical of BODIPY moieties (Figure S3). In the non-coordinating solvent dichloromethane, **IrBDP** is poorly emissive. In a structurally related complex, such fluorescence quenching was shown to arise from a photoinduced electron transfer (PET) mechanism where the BODIPY fragment

acts as electron acceptor and the iridium center as electron donor upon photoexcitation.[25] In contrast, **IrBDP** became highly emissive in DMSO with a quantum yield of 20.8 ± 1.4 %, that is close to that of the ligand precursor **phox-BDP** (25.6 ± 1.6% in MeOH) and a maximum at ca. 510 nm.

Since this family of complexes is known to undergo chlorido ligand exchange, the stability of **IrBDP** was examined by ^1H NMR in DMSO-d^6 at room temperature. Rapid exchange of the chlorido ligand to DMSO took place (half-life ca. 30 min), leading to the formation of a cationic species (**IrBDP$^+$**). At equilibrium (reached in ca. 5 h), the **IrBDP/IrBDP$^+$** ratio was 4:96 (Figure S2). Thus, the bright green fluorescence emission observed in DMSO accounts for the cationic complex **IrBDP$^+$** (Supplementary video 1). Fluorescence emission intensity of **IrBDP$^+$** appeared to be related to the solvent viscosity (CH_2Cl_2 > water > DMSO > glycerol, Figure S3).[26] This feature is characteristic of BODIPY-based molecular rotors with an aryl substituent at the *meso* position for which both fluorescence intensity and lifetime depend on viscosity. However, the presence of methyl substituents at positions 1, 3, 5 and 7 of the BODIPY core made the viscosity response modest (x = 0.18) in agreement with the literature.[27]

As the stock solution of **IrBDP** is prepared in DMSO, all the following experiments are carried out using the exchanged form **IrBDP$^+$** except for reactivity studies. Prior to cell assays, the octanol-water partition coefficient (log P) of **IrBDP$^+$** was determined to be 0.95 by the classical "shake flask" method using absorption readout.[28] This result is in agreement with previously reported half-sandwich complexes with values ranging from -0.95 to 4.2,[20,29] confirming the relatively low lipophilic nature of this cationic species. Nevertheless, the formation of an *aqua* complex during this experimental setup cannot be ruled out. Hence, since the speciation of iridium is hard to define in complex media, the different forms will next be collectively named **IrBDP**.

Cell toxicity of IrBDP. Cell response to **IrBDP** was monitored by a label-free viability assay based on impedance readout using the xCELLigence® Real Time Cell Analysis (RTCA) system. Experiments were performed using two cell types, HeLa as a model of cancerous cells and hTERT-RPE1 as a model of non-tumoral cells (Figure S4). Concentration-dependent changes of the cell index were observed for both cell lines with a rapid drop for the two highest concentrations of **IrBDP**, suggesting a loss of adhesion followed by a recovery period (shorter for hTERT-RPE1 cells) and cell proliferation (**Figure 2a**). Accordingly, the IC$_{50}$ of **IrBDP** in HeLa and hTERT-RPE1 cells was found equal to 8.6 ± 1.0 µM and 11.1 ± 0.7 µM at 48 h of treatment by the classical MTT assay.

a.

b.

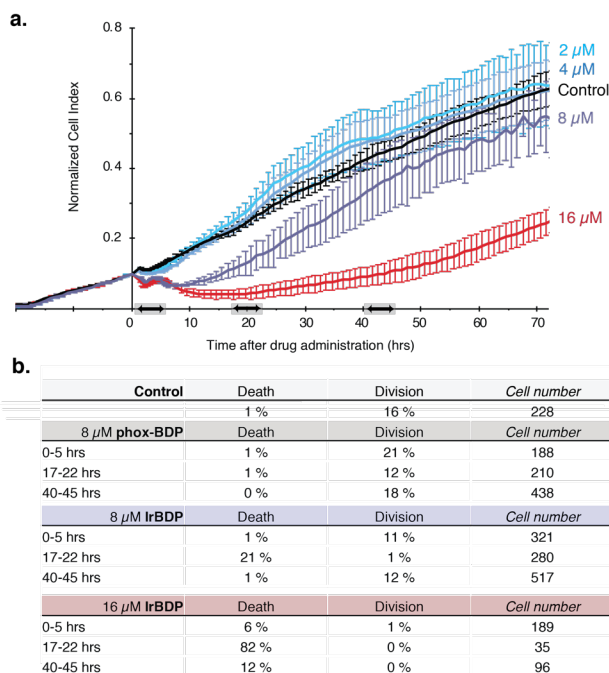| Control	Death	Division	Cell number
	1 %	16 %	228
8 μM phox-BDP	Death	Division	Cell number
0-5 hrs	1 %	21 %	188
17-22 hrs	1 %	12 %	210
40-45 hrs	0 %	18 %	438
8 μM IrBDP	Death	Division	Cell number
0-5 hrs	1 %	11 %	321
17-22 hrs	21 %	1 %	280
40-45 hrs	1 %	12 %	517
16 μM IrBDP	Death	Division	Cell number
0-5 hrs	6 %	1 %	189
17-22 hrs	82 %	0 %	35
40-45 hrs	12 %	0 %	96

Figure 2. Dose-dependent inhibition of cell proliferation and cell death upon **IrBDP** treatment. **a.** Real time monitoring of HeLa cell proliferation at the indicated **IrBDP** concentrations (RTCA xCELLigence®). Cell index profiles (Mean ± SD, triplicates) of treated or control cells (DMSO vehicle). Normalization at time of **IrBDP** administration. **b.** Percentages of cells dividing or dying over 5-h periods from 0-, 17- and 40-h after addition of **IrBDP** or **phox-BDP** as control. Events were counted on phase contrast videos (see also supplementary videos 2 and 3).

To provide an interpretation of the RTCA profiles, the behavior of HeLa cells was monitored in parallel by time lapse videomicroscopy and the percentages of cells dividing or dying over a 5-h period from 0-, 17- and 40-h after addition of **IrBDP** or **phox-BDP** as a control were calculated (**Figure 2b**). Cells treated by **phox-BDP** displayed division and death rates comparable to those of cells treated with vehicle, demonstrating its lack of toxicity. Conversely, 16 μM **IrBDP** (2 x IC$_{50}$) drastically inhibited cell division and induced cell death with the highest proportion observed between 17 and 22 h after drug addition. Cells exposed to 8 μM **IrBDP** (1 x IC$_{50}$) showed an immediate but transient loss of cell adhesion (between 0 and 5 h). While cell division was almost completely abolished and 20 % of cells died between 17 and 22 h after 8 μM **IrBDP** addition, 80 % cells remained adherent and eventually divided although at a lower rate as observed between 40 and 45 h. Further experiments are needed to determine whether and how cells are able to counterbalance **IrBDP** toxicity.

Cellular uptake and distribution of IrBDP. Taking advantage of the luminescence properties of **IrBDP**, its cell uptake was first monitored by time-lapse fluorescence microscopy in living HeLa cells over a period of 30 min (Figure S5a). The green fluorescence emission corresponding to internalized **IrBDP** was detectable as soon as 3 min after drug administration. This extremely fast uptake rate is reminiscent of our previously reported fluorescent iridium complex, in which the BODIPY moiety was appended on the labile position.[21] Intracellular accumulation of **IrBDP** in HeLa treated with 10 μM **IrBDP** for 30 min was independently confirmed by assaying the iridium concentration by ICP-OES which equalled 307 ± 8 ng/10^6 cells. A similar value of 440 ± 7 ng/10^6 cells was measured in hTERT-RPE1 cells.

We further investigated the subcellular distribution of **IrBDP** by confocal microscopy. Fixed HeLa and hTERT-RPE1 cells stained with 8 μM **IrBDP** for 1 h were used to measure spatially resolved fluorescence spectra (Figure S5b) demonstrating that the spectra of **IrBDP** emission obtained *in vitro* and in the intracellular context were identical. Besides, the position of the emission band at 520 nm was identical regardless of the region of interest or the cell line.

To get insight into the mechanism of **IrBDP** internalization, we examined if the metabolic inhibitors 2-deoxyglucose or oligomycin altered **IrBDP** intracellular accumulation (Figure S6b). Flow cytometry analysis of HeLa cells showed that ATP depletion did not prevent **IrBDP** intracellular accumulation, demonstrating that cell uptake mostly occurs by passive diffusion through the plasma membrane, in accordance with previous observations.[29] Consistently, **IrBDP** staining of intracellular structures was insensitive to aldehyde fixation (Figure S6a). We also compared the staining patterns of **IrBDP** with the ligand **phox-BDP**, devoid of iridium. **IrBDP** reproducibly located to large organelles excluding the nucleus. In contrast, live and fixed cells administered with **phox-BDP** exhibited bright medium size vesicles, similar to BODIPY-based lipid droplet dyes' staining pattern.[30] Finally, **IrBDP** could be detected neither in the plasma membrane nor in early or late endosomes labeled with EEA1 and LBPA antibodies respectively (Figure S7), thus indicating that endocytosis is not a major route for **IrBDP** internalization.

Intracellular distribution of IrBDP. Time-lapse fluorescence microscopy in living HeLa cells exposed to **IrBDP** showed a quasi-immediate accumulation of the compound in intracellular membranes accompanied by the progressive appearance of bright puncta (Figure S5c). To identify these structures, cells were stained with a range of organelle-specific fluorescent probes prior to **IrBDP** addition. We used DRAQ5 or Hoechst 33342 for the nucleus, ER-tracker Red (ERTR) for the endoplasmic reticulum (ER), Mitotracker Red (MTR) for mitochondria and Lysotracker Red (LTR) for lysosomes. We noticed that the order of addition of the molecules mattered since, when **IrBDP** was administered prior to MTR (Figure S8a), a significant loss of MTR signal was observed. Hence, **IrBDP** presumably precluded MTR to accumulate in the mitochondria, suggesting competition between the two molecules.[31]

Figure 3 shows that **IrBDP** was retained in the ER membrane as seen by its colocalization with ERTR. In addition, the numerous intense bright puncta also colocalized with the ER signal. As the fluorescence intensity of **IrBDP** is enhanced in a viscous environment (see above), we hypothesized that these bright spots could be lipid droplets (LD), known to be generated in the ER membrane.[32] In order to confirm this hypothesis, HeLa cells were cultured with oleic acid (OA) supplemented with BDP-C12 to trigger the formation of red-fluorescent LDs. During the last hour of treatment, **IrBDP** was added. We observed that **IrBDP** stained all LDs identified by BDP-C12 fluorescence. The ratio between **IrBDP** and BDP-C12 staining varies amongst LDs, likely due to the sequential addition of the dyes (Figure 3b).

In conclusion, under these conditions, **IrBDP** can be incorporated into pre-existing LDs as well as LDs budding from the ER membrane during the last hour of treatment, the ER acting as a reservoir of **IrBDP**. To analyze the dynamic behavior of **IrBDP** in the long term in the absence of oleic acid as a trigger to LD formation, HeLa cells were pulse labeled with **IrBDP** for 45 min, then washed and observed over 16 h by time-lapse videomicroscopy (supplementary movie 4 and snapshots in Figure S5c). The progressive appearance of bright puncta assigned to LDs was observed over time indicating that **IrBDP** accompanied lipids in their intracellular route. Meanwhile, the ER and mitochondria staining did not faint, suggesting that part of **IrBDP** was continuously retained.
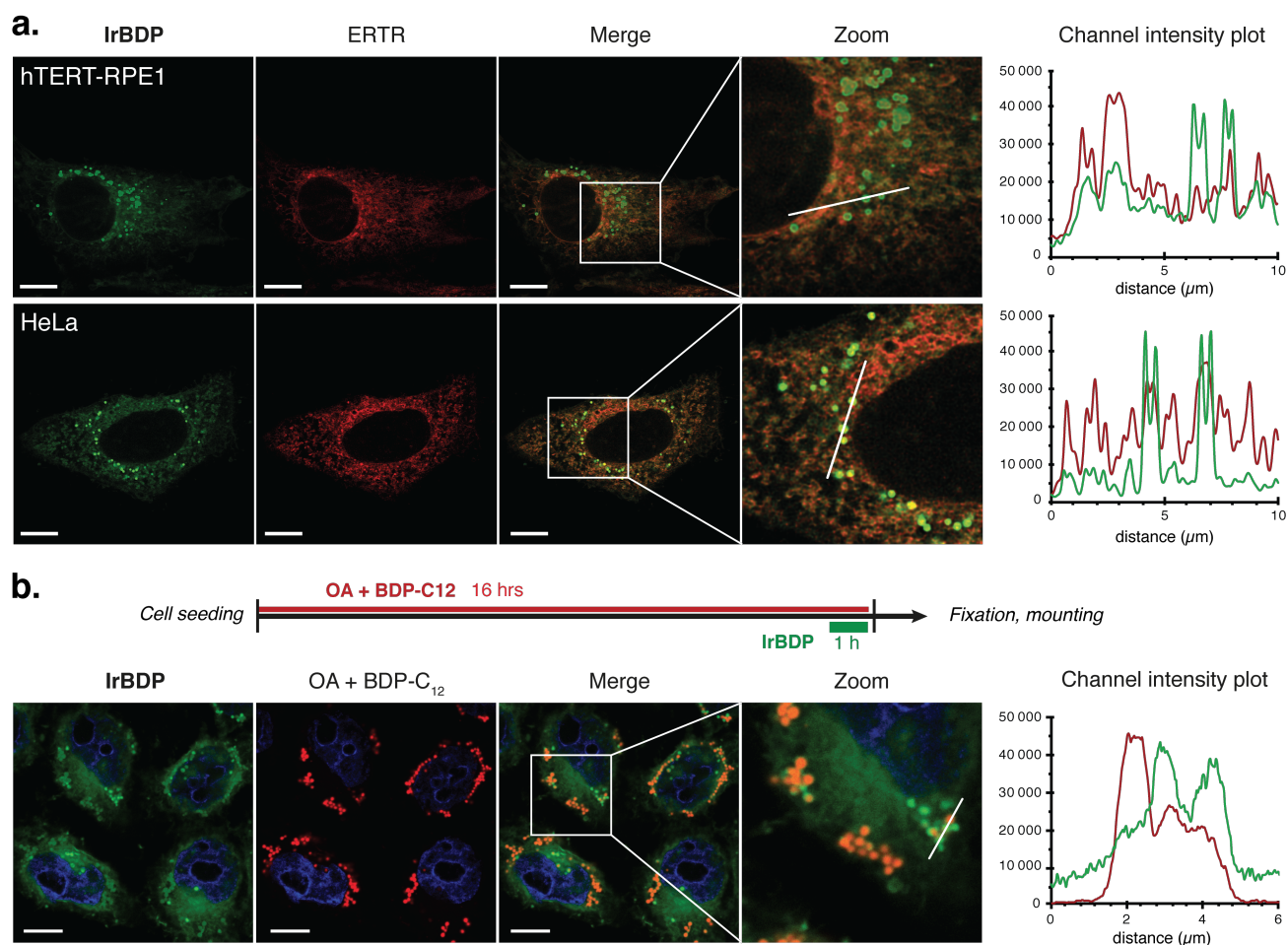

Figure 3. IrBDP accumulates in the ER and LDs, imaged by confocal microscopy. **a.** Cells were sequentially incubated with ERTR (red) for 15 min to label the ER and with 10 μM **IrBDP** (green) for 15 min. Channel intensity plots along a 10 μm line are shown on the right. **b.** Cells were exposed to 100 μM oleic acid (OA) and 1 μM BDP-C12 (red) for 16 h to induce the formation of fluorescent LDs followed by exposure to 10 μM **IrBDP** (green) for 1 h. DNA was stained with Hoechst 33342 (blue). Colocalization is shown in orange. Scale bar 10 μm

As previous studies showed accumulation of structurally related complexes to mitochondria[33] or lysosomes[34], we also examined whether **IrBDP** was retained in these organelles. All mitochondria were labeled by **IrBDP** (Figure S8b), suggesting a tropism to mitochondrial membrane consistent with its lipophilic and cationic nature. In contrast, **IrBDP** was only detected in a small percentage of lysosome structures with a high cellular heterogeneity (Figure S9a). This labeling was stable over time up to 6 h after **IrBDP** addition (Figure S9b), indicating that **IrBDP** was not directly addressed to lysosomes but could rather traffic to lysosomes through LDs.[35] Indeed, mature droplets are known to detach from the ER membrane and interact with other organelles in the context of lipid trafficking and energy metabolism.[36] Biogenesis of LDs can also be related to oxidative and/or ER stress.[36,37] In this context, LDs allow transport of exogenous hydrophobic molecules, misfolded proteins or lipids to degradative compartments. The distribution of LDs charged with **IrBDP** was analyzed on 3D-reconstructed cells and their proximity to mitochondria and lysosomes was examined (**Figure 4**). Both cell lines exhibited LDs close to mitochondria (68-78%) and lysosomes (23-30%), supporting the idea that LDs could act as a vehicle to incidentally deliver **IrBDP** to both these organelles.

To summarize, upon cell uptake, **IrBDP** mainly locates to the ER and mitochondria. Budding of lipid droplets from the ER appears as an alternative route to deliver **IrBDP** to other organelles such as the lysosome.
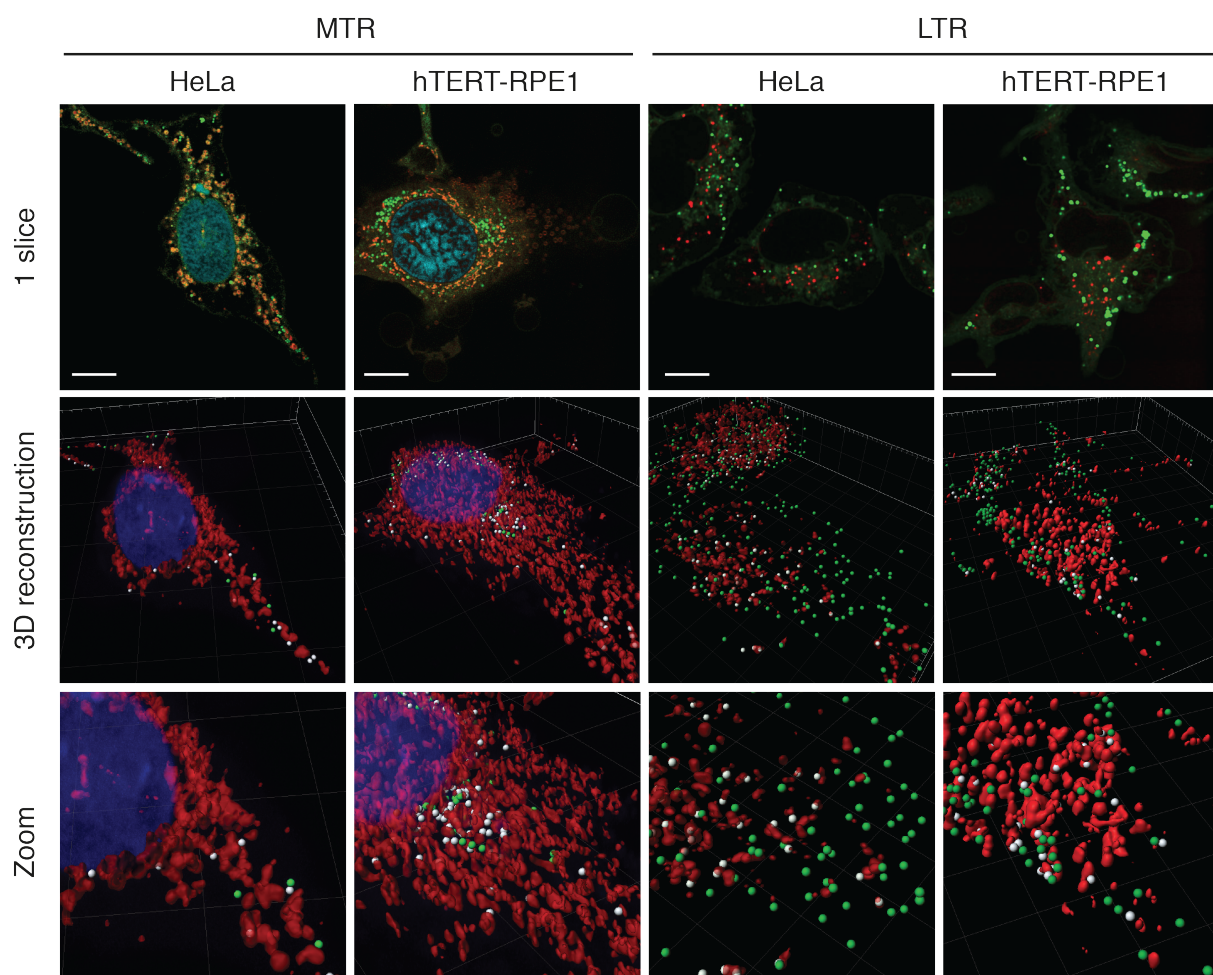

Figure 4. LDs charged with **IrBDP** are located in the vicinity of mitochondria and lysosomes, imaged by confocal microscopy on live cells. Cells were incubated for 15 min with **IrBDP** (green) after staining with the indicated tracker (red) to label either mitochondria (MTR) or lysosomes (LTR). 210 nm slices and 3D reconstructions of 31, 47, 50 and 44 slices respectively are shown. LDs are modeled as spheres and organelles as red surfaces in Imaris software. LDs interacting with organelles are highlighted in white (0.5 μm distance threshold). Scale bar and grid: 10 μm.

5

IrBDP causes ER-stress and disrupts Golgi structure. The accumulation of **IrBDP** in the ER prompted us to get a closer look at the cellular response. HeLa cells treated with **IrBDP** for several hours and monitored by phase contrast videomicroscopy transiently displayed refrigent vesicles that increased in size and eventually merged over time (supplementary video 3), this morphology being similar to cytoplasmic vacuoles.[38] **IrBDP** was not detected in these vacuoles but some of them were found positive for LAMP1 and LC3B suggesting that they derive from the endosomal-lysosomal compartment and autophagosomes. However, they were not stained by LTR, demonstrating that they were non-acidic and thus non-functional (Figure S10). Cytoplasmic vacuolization can be the consequence of ER or Golgi stresses.

The ER constitutes the major membrane trafficking system. Several metallodrugs are known to generate ER stress[39] which switches on a signaling network termed the Unfolded Protein Response (UPR) to relieve this stress. The UPR relies on three key signal activators, inositol-requiring protein 1 (IRE1), protein kinase RNA-like ER kinase (PERK) and activating transcription factor 6 (ATF6) that define three downstream pathways. In normal conditions, these three sensors are retained by the chaperone GRP78 on the ER membrane. To investigate whether **IrBDP** accumulation in the ER elicited the UPR, we analyzed key molecules pertaining to the three branches of the UPR.

As a general feature of UPR activation, we found that GRP78 accumulated over several hours of treatment on the HeLa cell line. The PERK branch of UPR was found activated as **IrBDP** also induced the shift of PERK (Figure S11a), suggesting its post-translational modification and activation. On both HeLa and hTERT-RPE1 cells, the phosphorylation of its substrate eIF2α[40,41] was observed, accounting for mRNA translation inhibition (**Figure 5a**). As expected, this resulted into nuclear accumulation of the downstream target ATF4 (Figure S11b).

On HeLa cells, the proapoptotic protein CHOP became upregulated concomitantly to the activation of caspase 3, marking the onset of apoptotic cell death. Moreover, a transient accumulation of the spliced form of XBP-1 indicated that the IRE1 branch of UPR was also detected in this cell line. Interestingly, neither CHOP nor IRE1 activation was observed in the hTERT-RPE1 cell line (Figure S12).

In contrast, ATF6 was not cleaved as expected but decreased upon **IrBDP** treatment in a dose-dependent manner (Figure S11a). Altogether these results show that **IrBDP** elicited an ER stress with incomplete UPR response. Since cleavage of ATF6 occurs in the Golgi apparatus,[42] we examined the morphology of the Golgi and the golgin GM130 status, responsible for the integrity of this organelle.[43] A rapid and dose-dependent disappearance of GM130 was observed by Western blot, suggesting either its degradation or conversion into an insoluble form (**Figure 5a**).
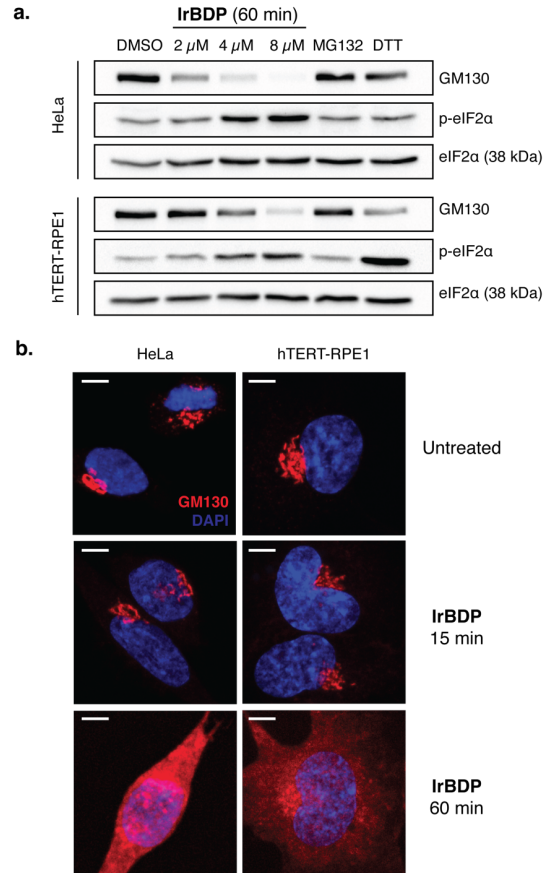

Figure 5. Cellular response to a 60 min treatment of HeLa and hTERT-RPE1 cells with **IrBDP**. **a.** Western blot analysis showing the loss of golgin GM130 and phosphorylation of eIF2-alpha in **IrBDP**-treated cells. DTT (2.5 mM, 30 min) and MG132 (1 μM, 60 min) were used as known ER-stress inducers[44]. **b.** Confocal z-projections showing dispersal of the Golgi apparatus (GM130 immunolabeling, red) detected after a 60 min treatment with 4 μM **IrBDP**. DAPI staining (blue). Scale bar = 5 μm.

The latter hypothesis was privileged, as the GM130 signal was not recovered upon proteasome inhibition (data not shown). Consistently, GM130 was still detected by immunofluorescence (**Figure 5b**). HeLa cells exhibited a striking Golgi dispersal whereas a modest effect was induced in hTERT-RPE1 cells. Therefore, in addition to ER stress, **IrBDP** alters the Golgi integrity, a phenotype that persisted up to 24 h in parallel with the onset of cell death as seen by cleavage of caspase-3 starting from 6 h of treatment of HeLa cells (Figure S12).

IrBDP covalently binds to amino acids and proteins. Hypothesizing that **IrBDP** can form covalent adducts with macromolecules at the labile position, in particular with S and N donor ligands,[45,46] its interaction with model amino acids was examined by mass spectrometry and fluorescence spectroscopy.
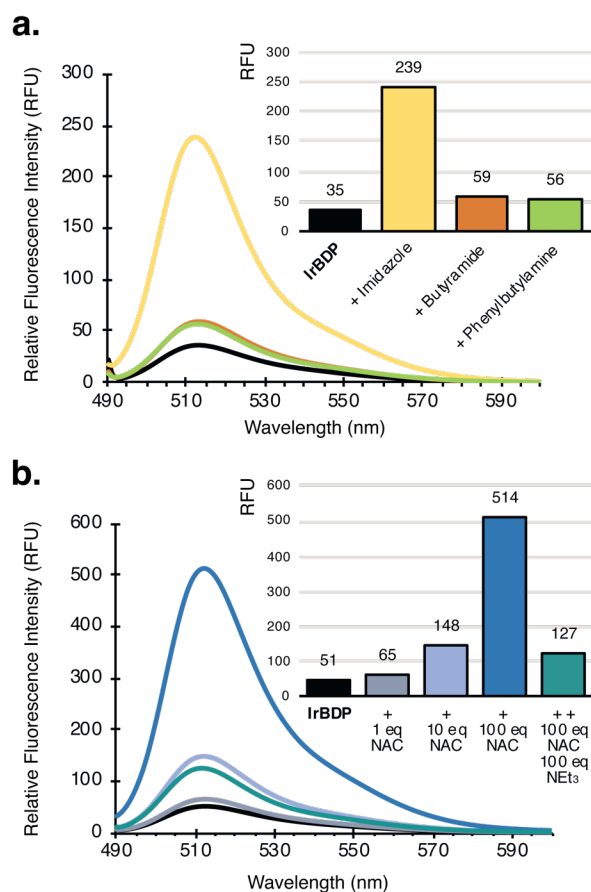
a.

b.

Figure 6. Emission spectra of **IrBDP** in CH_2Cl_2 (exc. 488 nm) incubated with **a.** stoichiometric amount of various substrates or **b.** with the indicated amount of NAC and NEt₃. NAC = N-AcCysOMe.

ESI-HRMS performed in positive ionization mode of **IrBDP** (in its chlorido form) in $MeOH/H_2O$ displayed two predominant peaks centered at *m/z* 720.2544 and *m/z* 744.2521, unambiguously ascribed to $[M - Cl]^+$ without and with the replacement of two fluorido substituents by two methoxy groups (shift of 23.9977 mass units, see MS spectra in ESI†). Stoichiometric mixtures of **IrBDP** and N-acetyl histidine, N-acetyl cysteine methyl ester, phenylbutylamine mimicking lysine and butyramide mimicking glutamine and asparagine were also analyzed after incubation at 37°C for 1 h. Adducts were only detected for the first three substrates with variable abundance (N-AcCysOMe > N-AcHis >> phenylbutylamine, Table S1 and Annex 3). The presence of water in the reaction medium may have favored the formation of these adducts via a transient *aqua* complex as already observed for this class of complexes.[6,47]

Reaction between **IrBDP** (in its chlorido form) and excess imidazole, N-AcCysOMe, butyramide or phenylbutylamide in CH_2Cl_2 was also investigated by fluorescence spectroscopy. As indicated above, **IrBDP** is poorly emissive in CH_2Cl_2 and the presence of excess amide and amine did not significantly change the fluorescence. In contrast, addition of excess imidazole or N-AcCysOMe resulted in a fluorescence enhancement (**Figure 6**). Both observations are consistent with the previously observed formation of cationic adducts by substitution of chlorido by imidazole or thiol group of N-AcCysOMe. Interestingly, in the presence of NEt₃, the fluorescence intensity of the reaction product with N-AcCysOMe was much weaker. This finding results from thiol deprotonation and subsequent formation of a neutral complex. To conclude, **IrBDP** is able to react with selected amino acids and the emission properties of the adduct depend on its charge.

We investigated the reactivity of **IrBDP** with proteins from cell extracts. For this, a HeLa whole protein extract obtained by solubilization with 1% Triton X-100 was incubated with 10 μM **IrBDP** at 37°C and proteins were separated by SDS-PAGE. The fluorescence and Coomassie blue staining patterns were compared and appeared nearly identical regardless of the incubation time. We conclude that **IrBDP** reacted indiscriminately with the vast majority of the proteins and remained strongly bound despite the harsh denaturing and reducing conditions used for sample preparation. Conversely, no fluorescence was detected on the lane corresponding to cell lysate sample treated with **phox-BDP** as it is unable to form covalent bonds with proteins (Figure S13).

To determine whether protein adducts could also be formed *in cellulo*, live HeLa and hTERT-RPE1 cells were incubated with 10 μM **IrBDP** for 1 h, harvested and lysed with 1% Triton X-100 and protein extracts were analyzed as above. In both cell lines and especially for the hTERT-RPE1 cell line, the fluorescence and Coomassie blue staining patterns were different, demonstrating that **IrBDP** formed adducts with specific proteins in these conditions (**Figure 7**). Identification of these protein adducts is presently challenging, but we could hypothesize that they are located in the ER and mitochondria where **IrBDP** showed preferential accumulation.[48]
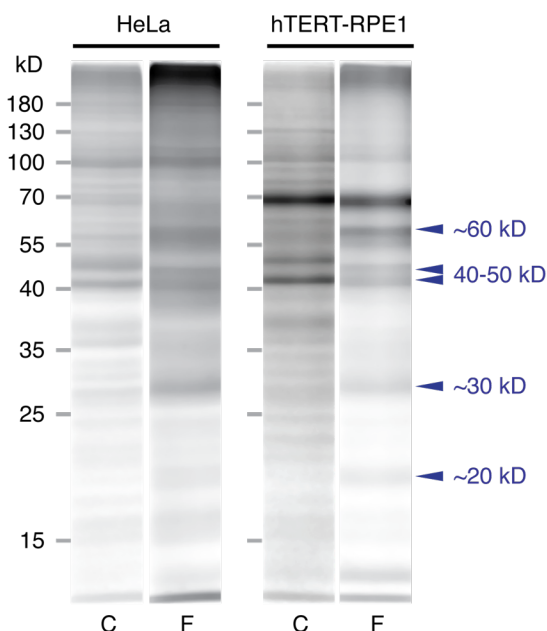
Figure 7. Visualization of **IrBDP** protein adducts after treatment of live HeLa and hTERT-RPE1 cells. Comparison of the Coomassie blue staining (C) and Fluorescence (F) profiles obtained after electrophoresis of 100 µg of proteins per lane. Proteins were separated by polyacrylamide gel electrophoresis under denaturing and reducing conditions. Arrows indicate intense fluorescent bands corresponding to low-abundance proteins, not detected after Coomassie blue staining.

CONCLUSION

In summary, we have reported the synthesis and characterization of a half-sandwich iridium complex comprising a 2-phenyloxazoline chelating ligand to which was appended a BODIPY moiety. We anticipated that this lipophilic entity would specifically address the complex to membrane-rich subcellular compartments such as the ER and mitochondria. As such, it might further exacerbate intracellular ROS production and overall cytotoxicity as these properties were previously highlighted for structurally related half-sandwich iridium complexes.

Furthermore, the bright fluorescence of BODIPY allowed us to track this complex in the intracellular context. Indeed, in its cationic form, **IrBDP** exhibits a bright green fluorescence. As demonstrated using confocal microscopy, the presence of a BODIPY on the complex drove its rapid accumulation into the ER and mitochondria after passive permeation through the plasma membrane, owing to its hydrophobic and cationic character. Afterwards, lipid droplets charged with **IrBDP** were observed, budding from the ER membrane[32] and acting as a vehicle to deliver **IrBDP** to other organelles including lysosomes[36].

Accumulation in the ER elicited the activation of several ER-stress sensors (PERK, GRP78, eIF2alpha, ATF4, XPB-1s) and thus presumably impaired its protein folding capacity. Moreover, intracellular trafficking seemed severely affected as a dose-dependent and irreversible dispersal of the Golgi apparatus was observed within one hour. As a consequence of ER and Golgi stresses, cytoplasmic vacuolization was noticed upon several hours of exposure to **IrBDP**. To the best of our knowledge, **IrBDP** is the first reported half-sandwich iridium complex inducing an ER-stress, all the iridium-based ER stress inducers belonging to the bis-cyclometalated family of complexes.[39,49] Altogether these results suggest a molecular mechanism leading to cell death, as evidenced via videomicroscopy, proliferation alteration and activation of caspase-3. Despite **IrBDP** being 2-fold less cytotoxic than previously reported **Ir-phox** complexes in terms of IC_{50} value,[7] tumor cells were repeatedly more sensitive to the complex than the non-tumoral hTERT-RPE1 cells.

Finally, owing to its labile coordination site, **IrBDP** readily reacts with imidazole, thiol and amine (to a lower extent) by formation of coordination bonds with sulfur or nitrogen donor ligands. This provides a mechanism by which **IrBDP** forms stable adducts with cellular proteins both *in vitro* and *in vivo*, explaining the persistence of **IrBDP** on ER and mitochondria structures. The identification of **IrBDP**-protein adducts will be our next step to understand how the chemical reactivity relates to the biological properties of this class of complexes. More generally, targeting cytotoxic iridium complexes to subcellular compartments could be further expanded by appending dedicated functional groups to the complex scaffold. For instance, replacing the BODIPY entity with an alkyl chain, sterols or sphingolipids could be a strategy to address piano-stool complexes to specific membrane subdomains.

EXPERIMENTAL SECTION

Synthetic procedures and compounds characterization. All compounds are >95% pure by HPLC. Reagents were purchased as reagent-grade and used without further purification. All reactions were performed under nitrogen atmosphere, were monitored by analytical TLC on silica gel 60 F254 plates 0.25 mm, and visualized under UV light (λ = 254 and 365 nm). Silica gel (SDS 60 ACC 35–70 mm) was used for column chromatography. NMR spectra were recorded on Bruker Avance III 300 MHz or 400 MHz spectrometers at room temperature. Chemical shifts (δ) are expressed in part per million (ppm), reported as s = singlet, d = doublet, t = triplet, m = multiplet; and referenced to the solvent peak of CD_2Cl_2 (^{13}C NMR: δ = 53.84 ppm; ^1H NMR: δ = 5.32 ppm). BDP-CHO was obtained from commercially available starting material using a previously described synthetic procedure.[50]

phox-BDP (4,4-Difluoro-8-(4-(4',5'-dihydrooxazole)phenyl)-1,3,5,7-tetramethyl-4-bora-3a,4a-diaza-s-indacene) Ethanolamine (10 µL, 170 µmol, 1.0 eq) was added to a solution of BDP-CHO (60 mg, 170 µmol, 1.0 eq) in 4 mL acetonitrile. The reaction mixture was stirred at room temperature during 5 h. DIB (66 mg, 204 µmol, 1.2 eq) was then added and stirring continued overnight. TLC monitoring showed a conversion of about 50% (Cy/AcOEt 7:3), water (ca. 5 mL)was added and the aqueous layer was extracted twice with CH_2Cl_2 (ca. 10 mL). The organic layer was

dried over $MgSO_4$ and concentrated under vacuum to afford 104 mg of crude product as a dark oil. The residue was purified by column chromatography (SiO_2 3.5 g, Cy/AcOEt 7:3) to yield the expected oxazoline as a light purple solid (30 mg, 76 µmol, 45 %). Rf(Cy/AcOEt 7:3) = 0.3. Purity: 94% (RP-HPLC). ^1H NMR (400 MHz, CD_2Cl_2) δ (ppm): 8.12 (d, 2H, J = 8.5 Hz, H2), 7.42 (d, 2H, J = 8.5 Hz, H3), 6.06 (s, 2H, H8), 4.49 (t, 2H, J = 9.7 Hz, H14), 4.10 (t, 2H, J = 9.5 Hz, H13), 2.55 (s, 6H, H11), 1.44 (s, 6H, H10). ^{13}C {^1H} NMR (101 MHz, CD_2Cl_2) δ (ppm): 164.20 (C12), 156.28(C9), 143.81(C7), 141.52(C5), 138.35(C1), 131.66(C6), 129.47(C2), 129.35(C4), 128.86(C3), 121.86(C8), 68.45(C14), 55.68(C13), 14.90(t, C11), 14.87(s, C10). HRMS (ESI+): m/z calculated for $C_{22}H_{22}BF_2N_3O$: 394.1897; found: 394.1897 [M+H]+ (0 ppm). Absolute quantum yield(%): 25.59 ± 1.647. (MeOH). Fluorescence color coordinates: x: 0.18852 ; y: 0.70484 ; u': 0.06805 ; v': 0.57247 Lifetime at lambda max (ns): MeOH: 2.18(87%), 3.40(4%), 0.08(10%) ; H_2O: 1.99(5%), 2.77(74%), 0.02(20%).

IrBDP (Chlorido(η^5-pentamethylcyclopentadienyl)(4,4-Difluoro-8-(4-(4',5'-dihydrooxazole-κN)phenyl-κC2)-1,3,5,7-tetramethyl-4-bora-3a,4a-diaza-s-indacene) Iridium (III)) [Cp*IrCl$_2$]$_2$ (22.1 mg, 28 µmol, 1.0 eq) and CH_3COONa (14 mg, 168 µmol, 6.0 eq) were added to a solution of phox-BDP in CH_2Cl_2 (24 mg, 61 µmol, 2.2 eq). The reaction mixture was stirred 3 days at room temperature under inert atmosphere. The reaction mixture was then filtered through a pad of Celite® 545 to afford the crude product after solvent removal. Purification was then carried out by column chromatography (SiO_2 6 g, CH_2Cl_2/AcOEt (5:5) + 1% Et_3N) to give a red solid (32 mg, 42 µmol, 76%). Purity: 97% (RP-HPLC). ^1H NMR (300 MHz, CD_2Cl_2) δ (ppm): 7.69 (s, 1H, H2), 7.55 (d, 1H, J = 7.7 Hz, H5), 6.97 (dd, 1H, J = 7.7, 1.2 Hz, H4), 6.07 (s, 1H, H14), 6.03 (s, 1H, H19) 4.91 (m, 2H, H9), 3.98-4.18 (m, 2H, H8), 2.56 (s, 6H, H16-17), 1.77 (s, 15H, HCp*), 1.62 (s, 3H, H12), 1.49 (s, 3H, H20). ^{13}C {^1H} NMR (75 MHz, CD_2Cl_2) δ (ppm): 179.61(C1), 164.95(C7), 155.49(C15), 154.21(C18), 144.79(C13), 143.09(C10), 142.51(C21), 138.01(C6), 134.21(C2), 131.65(C3), 126.20(C5), 121.19(C14), 120.96(C4), 120.54(C19), 87.85(C^{Cp^*}), 71.73(C9), 50.51(C8), 38.08, 31.06(C12), 29.67, 14.57-14.30-13.98(C16,C17,C20), 9.14($CH_3^{Cp^*}$). HRMS (ESI+): m/z calculated for $C_{32}H_{36}BClF_2IrN_3O$: 720.2543; found: 720.2550 [M-Cl]+ (1 ppm). Fluorescence data of [**IrBDP**]-DMSO exchanged complex: Absolute quantum yield(%): 20.82 ± 1.377 (MeOH). Fluorescence color coordinates: x: 0.19134 ; y: 0.71648 ; u': 0.06824 ; v': 0.57497. Lifetime at lambda max (ns): DMSO: 0.03(6%), 2.73(70%), 3.28 (24%); H_2O: 5.00(1%), 2.93(92%), 0.08 (7%).

Mass spectrometry analysis. ESI-MS experiments were carried out using a LTQ-Orbitrap XL from Thermo Scientific (Thermo Fisher Scientific, Courtaboeuf, France) and operated in positive ionization mode, with a spray voltage at 3.6 kV. Sheath and auxiliary gas were set at a flow rate of 45 and 15 arbitrary units (a.u.), respectively. Applied voltages were 20 and 70 V for the ion transfer capillary and the tube lens, respectively. The ion transfer capillary was held at 275°C. Detection was achieved in the Orbitrap with a resolution set to 100,000 (at m/z 400) and a m/z range between 200-1000 in profile mode. Spectrum was analyzed using the acquisition software XCalibur 2.1 (Thermo Fisher Scientific, Courtaboeuf, France). The automatic gain control (AGC) allowed accumulation of up to 2.10^5 ions for FTMS scans, Maximum injection time was set to 500 ms and 1 µscan was acquired. 5 or 20 µL were injected using a Thermo Finnigan Surveyor HPLC system (Thermo Fisher Scientific, Courtaboeuf, France) with a continuous infusion of methanol or methanol/water mixture at 100 µL/min.

Photophysical properties. Solutions of **IrBDP** and **phox-BDP** were prepared in various solvents (Table S2). To prepare **IrBDP$^+$**, **IrBDP** was dissolved in DMSO and equilibrated for 24 h prior to dilution in various solvents (Table S2). Electronic absorption spectra were recorded on a Cary50 spectrophotometer (Varian) in 1-cm pathlength quartz cuvettes at 20°C. Steady-state fluorescence emission spectra were recorded on a FP-6200 spectrofluorimeter (Jasco) at 20°C with excitation set at 488 nm. Excitation and emission bandwidths were set to 5 nm and scan rate to 125 nm/min. Fluorescence lifetimes were measured on a Fluoromax-4

spectrofluorimeter equipped with a TCSPC accessory (Horiba) using the time domain technique. Absolute fluorescence quantum yields were measured on the same spectrofluorimeter equipped with the Quanta integrating sphere.

Log P$_{o/w}$ determination. Log P of **IrBDP$^+$** was determined using the "shake-flask" method from OCDE guideline n°107. Octanol-saturated water (OSW) and water-saturated octanol (WSO) were prepared using analytical grade octanol and ultrapure water. Aliquots of stock solutions of **IrBDP** in WSO were added to equal volumes of OSW in triplicate. Mixing was done by tube rotation for 5 min at ambient temperature to establish the partition equilibrium. Phase separation was performed by centrifugation at 3000 g for 5 min. [**IrBDP**]$_{WSO}$ was determined by absorbance readout using its molar extinction coefficient at 500 nm and a reference solution (ϵ_{WSO} = 43500 $l.mol^{-1}.cm^{-1}$). Partition coefficient of **IrBDP** was calculated using the equation: log P = log ([**IrBDP**]$_{WSO}$/[**IrBDP**]$_{OSW}$).

Cell culture and viability assay. For all biological assays, stock solutions of 10 mM **IrBDP** and 1 mM **phox-BDP** were equilibrated for 24 h in DMSO and then diluted in the culture medium prior to administration. HeLa and hTERT-RPE1 cell lines were obtained from the American Type Culture Collection and cultured in DMEM Glutamax High Glucose and DMEM/F12 Glutamax respectively. Both media were supplemented with antibiotics (penicillin, streptomycin) and 10 % FBS, and were later referred to as complete medium. Long term treatments with **phox-BDP** and **IrBDP** were performed in media containing 5% FBS. Treatments for less than 1 h with **phox-BDP** and **IrBDP** were performed in serum-free media. All culture reagents and mounting medium were purchased from Invitrogen.

MTT Viability Assay: The cell proliferation assay was carried out using Promega CellTiter 96 Non-Radioactive Cell Proliferation Assay according to the supplier's protocol. Briefly, 4,000 HeLa or hTERT-RPE1 cells were seeded in 96-well plates and cultured in the presence of a range of 8 concentrations of **IrBDP** for 48 h in triplicate. MTT Dye Solution (15 µL) was added to each well and the plates were incubated at 37°C in a humidified 5 % CO_2 atmosphere for 4 h. Stop Solution (100 µL) was added to each well and absorbance was read at 570 nm using Infinite F200 PRO Tecan plate reader, once formazan crystals completely solubilized. Compound concentrations that produced 50% growth inhibition (IC_{50}) were calculated from non-linear regressions of the triplicate data using Graphpad Prism software.

RTCA and time-lapse videomicroscopy. xCELLigence E-plates were calibrated for a baseline definition and cells were seeded at 2,000 cells per well in 100 µL complete medium. After 24 h, **IrBDP** was added to a final concentration of 16, 8, 4, and 2 µM in triplicate and the cell index was measured over a period of 72 h (Real Time Cell Analyzer, Agilent). In parallel, 25,000 cells were seeded in 24-well plates and treated with either **IrBDP, phox-BDP** or DMSO as control. The cell behavior was monitored in real time by differential phase contrast videomicroscopy using an Olympus IX83 inverted microscope with 20x objective. Images were recorded over 5 h starting either immediately, 16 h or 40 h after treatment. At the end point, a green-fluorescence acquisition was made using a 488-nm excitation LED. Time-lapse movies (1 frame per 5 min) were processed using Fiji (Supplementary videos 2 and 3).

ICP-OES analysis. Briefly, 10 mm culture dishes were seeded with 250,000 HeLa or hTERT-RPE1 cells in complete medium. After two days, each dish was washed with warm PBS and cells were incubated with 10 mL of serum-free medium containing 10 µM **IrBDP** for 30 min. Supernatants were collected, cells were washed twice with PBS and harvested. Cell samples were digested ca. 1 h in ultrasonic bath with concentrated HNO_3 and 1% Triton X-100, and the extract was diluted with ultrapure water to a final volume of 5 mL and 2 %v/v HNO_3. Samples were filtered through 0.2 µm nylon filters and analyzed by ICP-OES. Iridium (212.681 nm, 3 replicates, read time 20 s) content was quantified using an ICP-OES 5100 SVDV Agilent instrument at ALIPP6 facility (ISTeP - Sorbonne Université). The concentrations used for calibration were 0, 8, 16, 31, 63, 125, 250, 500 and 1000 ppb. Plasma and nebulizer flows were 12 and 0.7 L/min respectively.

Live cell staining and immunofluorescence. Time-lapse phase contrast and fluorescence microscopy were performed using an Olympus IX83 inverted microscope with 40x objective. Confocal images were acquired using a Leica SP5 inverted confocal microscope with 63x immersive objective and 405 (DAPI, Hoechst 33342), 488 (**IrBDP**), 561 (Alexa 568, LTR, MTR, ERTR) and 633 nm (DRAQ5) Argon laser excitations with 63x objective. Fluorescence spectra in cells were recorded using the same confocal microscope with 488 nm laser excitation and 63x objective. A hybrid detector in photon-counting mode with a 5 nm bandwidth and 3 nm detection step size was used on a confocal slice of HeLa and RPE cells treated with 8 μM **IrBDP**.

Internalization of IrBDP. HeLa and hTERT-RPE1 cells were cultured in Millicell 8-well EZ-slides and stained with 1 μM **IrBDP** or **phox-BDP** for 30 min at 37°C either before or after fixation using 4% PFA and 3 PBS washes. The slide was mounted with Invitrogen Vibrance Vectashield Mounting Medium and imaged using a Leica SP2 upright confocal microscope with a 488 nm argon laser excitation. Alternatively, 10^6 cells were exposed for 30 min to 50 mM 2-deoxyglucose or 5 μM oligomycin prior to addition of 5 μM IrBDP for 15 min. Cells were trypsinized, fixed with 4 % PFA for 15 min, then washed and analyzed by flow cytometry.

Endoplasmic reticulum, mitochondria and lysosome staining. 8-well IBIDI slides were seeded with 7,500 HeLa or hTERT-RPE1 cells and cultured in 300 μL complete medium overnight at 37°C 5 % CO_2 in a humidified atmosphere. Cells were washed with PBS and stained in serum-free medium with ERTR (CellNavigator ER-Tracker Red, 30 min), MTR (100 nM Mitotracker Red CMX-Ros + DRAQ5, Invitrogen, 20 min) or LTR (50 nM Lysotracker Red DND-99, Invitrogen, 20 min) for the indicated time at 37°C 5%CO_2. Afterwards, staining media were replaced with serum-free medium containing 10 μM **IrBDP** for 15 min in the same conditions. Live cells (MTR, LTR) were imaged in serum-free medium containing 15 mM HEPES. Samples stained with ERTR were fixed *in situ* with 4% PFA in PBS and washed three times prior to acquisition by confocal microscopy.

Lipid Droplets staining. HeLa cells were seeded on 14 mm coverslips (25,000 cells per cm^2) and incubated in complete medium at 37°C, 5%CO_2 in a humidified atmosphere. After 24 h , cells were exposed to 100 μM Oleic Acid + 1 μM BDP-C12 for 16 h using supplementing FBS (prepared by sonication) at 10% in serum-free DMEM. During the last hour of treatment, **IrBDP** was added to a concentration of 10 μM. Cells were fixed with 4 % PFA in PBS and nuclei were stained simultaneously with 1 μg/mL Hoechst 33342. Coverslips were washed 3 times, mounted using Prolong Diamond mounting medium and imaged by confocal microscopy.

Immunofluorescence co-labelling. HeLa cells were seeded on 14 mm coverslips (25,000 cells per cm^2) and incubated in complete medium at 37°C 5%CO_2 in a humidified atmosphere. After 24 h, cells were treated with **IrBDP** and Bafilomycin as indicated or 0.1 % DMSO in serum-free media. Cells were fixed with 4% PFA in PBS and washed 3 times with PBS. Samples were blocked and permeabilized using 3% BSA and 0.5 % Triton X-100 in PBS for 30 min at room temperature. Coverslips were incubated overnight with primary antibody (1:100) in PBS 3 % BSA at 4°C, then for 1 h at room temperature with Alexa Fluor 568 secondary antibody (1:500 in PBS) and finally with 1 μg/mL Hoechst 33342 in PBS for 10 min. Coverslips were mounted using Prolong Diamond mounting medium. Primary antibodies: rabbit anti-ATF4 (D4B8 Cell Signaling #11815), mouse anti-EEA1 (BD-Transduction 610457), mouse anti-GM130 (BD Transduction 610823), rabbit anti-LC3B (Sigma L7543), rabbit anti-LAMP1 (Cell Signaling #9091), mouse anti-LBPA (6C4 Sigma T837). Secondary antibodies (Invitrogen): A-11031 goat anti-mouse IgG (H+L) Alexa Fluor 568 and A-11011 goat anti-rabbit Ig-G (H+L) Alexa Fluor 568.

Western Blots. Briefly, 10^6 cells were seeded in 60 mm culture dishes, incubated for 16 h in complete medium at 37°C 5% CO_2 in a humidified atmosphere and washed twice with PBS prior to **IrBDP** treatment in serum-free medium at the indicated concentration and time. Cells exposed to 0.1% DMSO and to 1 μM MG132 (1 h) or 2.5 mM DTT (30 min) were used as negative and positive controls respectively. Cells were harvested in cold PBS and lysed in RIPA buffer, supplemented with protease and phosphatase inhibitors. Protein titration was carried out using the microBCA assay-kit (based on Pierce BCA). Samples were analyzed by SDS-PAGE on polyacrylamide gels and transferred onto 20 μm nitrocellulose membranes. Membranes were blocked and incubated with primary antibody overnight at 4°C, HRP conjugated secondary antibody for 1 h at room temperature and the BioRad ECL (luminol) detection kit. Primary antibodies: Mouse anti-GM130 (BD Transduction #610823). Rabbit anti-phospho-eIF2-alpha (Ser51) (Cell Signaling #9721). Rabbit-anti-eIF2-alpha (Cell Signaling #9722). Rabbit anti-PERK/EIF2AK3 (Proteintech 20582-1-AP). Rabbit anti-ATF6 (Proteintech 24169-1-AP). Rabbit anti-GRP78 (Proteintech 11587-1-AP). Mouse anti-CHOP (L63F7 Cell Signaling #2895). Rabbit XBP-1-s (BioLegend # 6475). Rabbit anti-Cleaved Caspase-3 (Asp175) (5A1E) (Cell Signaling #9664). Mouse anti-β-Actin (Cell Signaling #4967). Secondary antibodies: HRP-conjugated anti-Mouse (Cell Signaling 7076) and anti-Rabbit IgG (Cell Signaling #7074).

SDS-PAGE electrophoresis, in vitro incubation with a cell lysate. A pellet containing 10^7 cells was mechanically broken in PBS 1% Triton X-100 (containing protease and metalloprotease inhibitors) at 4°C with a Dounce homogenizer. Proteins were titrated using the microBCA assay-kit (ca. 6.8 mg/mL) and the sample was split into 200 μg fractions (representing 1.1 million cells each) for the following treatments: vehicle (0, 1 and 3 h), 110 nmol **IrBDP** (1 and 3 h), 11 nmol **phox-BDP** at 37°C. All samples were then centrifuged 30 min at 21,000 g and 4°C resulting in a pellet and a supernatant (soluble fraction) that were both denatured using non-reductive Laëmmli buffers for 20 min at 95°C. Equal volumes corresponding to 32 μg of proteins from the supernatant fraction were migrated by SDS-Page electrophoresis on a 12% polyacrylamide gel. Gels were fixed overnight at 4°C with a mixture H_2O:EtOH:AcOH (4:5:1) and fluorescence was acquired using a Bio-Rad Chemidoc XRS+ with a UV trans-illumination and a green filter. The gel was then stained with Coomassie blue (2 h, room temperature) for another acquisition with a white trans-illumination and a green filter.

SDS-PAGE electrophoresis, treatment of live cells with IrBDP. A 6-well plate was seeded with 500,000 HeLa or hTERT-RPE1 cells in complete medium. The day after, each well was washed three times with hot PBS and media were replaced with serum-free media containing 100 nmol **IrBDP** for 1 h at 37°C 5%CO_2 in a humidified atmosphere. Media were discarded and cells were directly scratched and harvested in 2x100 μL PBS 1% Triton X-100 containing protease and metalloprotease inhibitors. DTT was added to a concentration of 1 mM and samples were centrifuged for 15 min at 14,000 g (4°C). The obtained supernatants were denatured for 5 min at 95°C and migrated by SDS-PAGE electrophoresis on a 12% polyacrylamide gel. The gel was fixed overnight at 4°C with a H_2O:EtOH:AcOH (4:5:1) mixture and fluorescence was acquired using a iBright Imager (Invitrogen) with a blue LED trans-illumination and a green filter. The gel was then stained with Coomassie blue (2 h, room temperature) for another acquisition of total protein content. Molecular weight analysis was performed using ImageLab (Bio-rad) and Fiji.

ASSOCIATED CONTENT

Supporting Information.

The following files are available free of charge.
- Supplementary figures S1-S13, tables S1-S3 and annexes (PDF)
- Supplementary video 1 (MP4)
- Supplementary videos 2, 3 and 4 (AVI)

AUTHOR INFORMATION

Corresponding Authors.

*† E-mail: michele.salmain@sorbonne-universite.fr
*‡ E-mail: joelle.sobczak@inserm.fr

ABBREVIATIONS USED

AcOEt, ethyl acetate; ATF, activating transcription factor; BODIPY, boron-dipyrromethene; CHOP, C/ERP-homologous protein 1; DAPI, 4',6-diamidino-2-phenylindole; DMEM, Dulbecco's Modified Eagle's Medium; EEA1, early endosome antigen 1; eIF2α, eukaryotic translation initiation factor 2A; ER, endoplasmic reticulum; ERTR, ER-tracker Red; FBS, fetal bovine serum; GRP78, binding-immunoglobulin protein or BiP; HRMS, high resolution mass spectrometry; ICP-OES, inductively coupled plasma optical emission spectrometry; IRE1, inositol requiring enzyme 1; LAMP1, lysosomal-associated membrane protein 1; LC3B, microtubule-associated protein light chain 3 B; LD, lipid droplets; LBPA, lysobisphosphatidic acid; LTR, Lysotracker Red; MTR, Mitotracker Red; NAC, N-Acetylcysteine methyl ester; OA, oleic acid; PFA, paraformaldehyde; PERK, PKR-like ER protein kinase; PET, photoinduced electron transfer; phox, 2-phenyloxazoline; RTCA, real-time cell analysis; SDS, sodium dodecyl sulfate; UPR, unfolded protein response; XBP-1s, X-box-binding protein 1, spliced isoform.

REFERENCES

(1) Konkankit, C. C.; Marker, S. C.; Knopf, K. M.; Wilson, J. J. Anticancer Activity of Complexes of the Third Row Transition Metals, Rhenium, Osmium, and Iridium. *Dalton Trans.* **2018**, *47* (30), 9934–9974. https://doi.org/10.1039/C8DT01858H.

(2) Caporale, C.; Massi, M. Cyclometalated Iridium(III) Complexes for Life Science. *Coord. Chem. Rev.* **2018**, *363*, 71–91. https://doi.org/10.1016/j.ccr.2018.02.006.

(3) Lord, R. M.; McGowan, P. C. Organometallic Iridium Arene Compounds: The Effects of *C*-Donor Ligands on Anticancer Activity. *Chem. Lett.* **2019**, *48* (8), 916–924. https://doi.org/10.1246/cl.190179.

(4) Anthony, E. J.; Bolitho, E. M.; Bridgewater, H. E.; Carter, O. W. L.; Donnelly, J. M.; Imberti, C.; Lant, E. C.; Lermyte, F.; Needham, R. J.; Palau, M.; Sadler, P. J.; Shi, H.; Wang, F.-X.; Zhang, W.-Y.; Zhang, Z. Metallodrugs Are Unique: Opportunities and Challenges of Discovery and Development. *Chem. Sci.* **2020**, *11* (48), 12888–12917. https://doi.org/10.1039/D0SC04082G.

(5) Roy, N.; Sen, U.; Ray Chaudhuri, S.; Muthukumar, V.; Moharana, P.; Paira, P.; Bose, B.; Gauthaman, A.; Moorthy, A. Mitochondria Specific Highly Cytoselective Iridium(III)–Cp* Dipyridophenazine (Dppz) Complexes as Cancer Cell Imaging Agents. *Dalton Trans.* **2021**, *50* (6), 2268–2283. https://doi.org/10.1039/D0DT03586F.

(6) Liu, Z.; Romero-Canelón, I.; Qamar, B.; Hearn, J. M.; Habtemariam, A.; Barry, N. P. E.; Pizarro, A. M.; Clarkson, G. J.; Sadler, P. J. The Potent Oxidant Anticancer Activity of Organoiridium Catalysts. *Angew. Chem. Int. Ed.* **2014**, *53* (15), 3941–3946. https://doi.org/10.1002/anie.201311161.

(7) Ramos, R.; Zimbron, J. M.; Thorimbert, S.; Chamoreau, L.-M.; Munier, A.; Botuha, C.; Karaiskou, A.; Salmain, M.; Sobczak-Thépot, J. Insights into the Antiproliferative Mechanism of (C^N)-Chelated Half-Sandwich Iridium Complexes. *Dalton Trans.* **2020**, *49* (48), 17635–17641. https://doi.org/10.1039/D0DT03414B.

(8) Zhang, W.-Y.; Banerjee, S.; Hughes, G. M.; Bridgewater, H. E.; Song, J.-I.; Breeze, B. G.; Clarkson, G. J.; Coverdale, J. P. C.; Sanchez-Cano, C.; Ponte, F.; Sicilia, E.; Sadler, P. J. Ligand-Centred Redox Activation of Inert Organoiridium Anticancer Catalysts. *Chem. Sci.* **2020**, *11* (21), 5466–5480. https://doi.org/10.1039/D0SC00897D.

(9) Hearn, J. M.; Hughes, G. M.; Romero-Canelón, I.; Munro, A. F.; Rubio-Ruiz, B.; Liu, Z.; Carragher, N. O.; Sadler, P. J. Pharmaco-Genomic Investigations of Organo-Iridium Anticancer Complexes Reveal Novel Mechanism of Action. *Metallomics* **2018**, *10* (1), 93–107. https://doi.org/10.1039/C7MT00242D.

(10) Xu, S.; Butkevich, A. N.; Yamada, R.; Zhou, Y.; Debnath, B.; Duncan, R.; Zandi, E.; Petasis, N. A.; Neamati, N. Discovery of an Orally Active Small-Molecule Irreversible Inhibitor of Protein Disulfide Isomerase for Ovarian Cancer Treatment. *Proc. Natl. Acad. Sci.* **2012**, *109* (40), 16348–16353. https://doi.org/10.1073/pnas.1205226109.

(11) Bodio, E.; Le Gendre, P.; Denat, F.; Goze, C. Development of Trackable Anticancer Agents Based on Metal Complexes. In *Advances in Inorganic Chemistry*; Elsevier, 2016; Vol. 68, pp 253–299. https://doi.org/10.1016/bs.adioch.2015.09.004.

(12) Samanta, S.; Yang, S.; Debnath, B.; Xue, D.; Kuang, Y.; Ramkumar, K.; Lee, A. S.; Ljungman, M.; Neamati, N. The Hydroxyquinoline Analogue YUM70 Inhibits GRP78 to Induce ER Stress–Mediated Apoptosis in Pancreatic Cancer. *Cancer Res.* **2021**, *81* (7), 1883–1895. https://doi.org/10.1158/0008-5472.CAN-20-1540.

(13) Ma, W.; Tian, Z.; Zhang, S.; He, X.; Li, J.; Xia, X.; Chen, X.; Liu, Z. Lysosome Targeted Drugs: Rhodamine B Modified N^N-Chelating Ligands for Half-Sandwich Iridium(III) Anticancer Complexes. *Inorg. Chem. Front.* **2018**, *5* (10), 2587–2597. https://doi.org/10.1039/C8QI00620B.

(14) Ma, W.; Guo, L.; Tian, Z.; Zhang, S.; He, X.; Li, J.; Yang, Y.; Liu, Z. Rhodamine-Modified Fluorescent Half-Sandwich Iridium and Ruthenium Complexes: Potential Application as Bioimaging and Anticancer Agents. *Dalton Trans.* **2019**, *48* (15), 4788–4793. https://doi.org/10.1039/C9DT00999J.

(15) Ma, W.; Ge, X.; Xu, Z.; Zhang, S.; He, X.; Li, J.; Xia, X.; Chen, X.; Liu, Z. Theranostic Lysosomal Targeting Anticancer and Antimetastatic Agents: Half-Sandwich Iridium(III) Rhodamine Complexes. *ACS Omega* **2019**, *4* (12), 15240–15248. https://doi.org/10.1021/acsomega.9b01863.

(16) Leite, A.; Silva, A. M. G.; Cunha-Silva, L.; de Castro, B.; Gameiro, P.; Rangel, M. Discrimination of Fluorescence Light-up Effects Induced by PH and Metal Ion Chelation on a

Spirocyclic Derivative of Rhodamine B. *Dalton Trans.* **2013**, *42* (17), 6110. https://doi.org/10.1039/c2dt32198j.

(17) Kowada, T.; Maeda, H.; Kikuchi, K. BODIPY-Based Probes for the Fluorescence Imaging of Biomolecules in Living Cells. *Chem. Soc. Rev.* **2015**, *44* (14), 4953–4972. https://doi.org/10.1039/C5CS00030K.

(18) Loudet, A.; Burgess, K. BODIPY Dyes and Their Derivatives: Syntheses and Spectroscopic Properties. *Chem. Rev.* **2007**, *107* (11), 4891–4932. https://doi.org/10.1021/cr078381n.

(19) Hu, R.; Gómez-Durán, C. F. A.; Lam, J. W. Y.; Belmonte-Vázquez, J. L.; Deng, C.; Chen, S.; Ye, R.; Peña-Cabrera, E.; Zhong, Y.; Wong, K. S.; Tang, B. Z. Synthesis, Solvatochromism, Aggregation-Induced Emission and Cell Imaging of Tetraphenylethene-Containing BODIPY Derivatives with Large Stokes Shifts. *Chem. Commun.* **2012**, *48* (81), 10099. https://doi.org/10.1039/c2cc35188a.

(20) Paitandi, R. P.; Mukhopadhyay, S.; Singh, R. S.; Sharma, V.; Mobin, S. M.; Pandey, D. S. Anticancer Activity of Iridium(III) Complexes Based on a Pyrazole-Appended Quinoline-Based BODIPY. *Inorg. Chem.* **2017**, *56* (20), 12232–12247. https://doi.org/10.1021/acs.inorgchem.7b01693.

(21) Zimbron, J. M.; Passador, K.; Gatin-Fraudet, B.; Bachelet, C.-M.; Plażuk, D.; Chamoreau, L.-M.; Botuha, C.; Thorimbert, S.; Salmain, M. Synthesis, Photophysical Properties, and Living Cell Imaging of Theranostic Half-Sandwich Iridium–4,4-Difluoro-4-Bora-3 *a* ,4 *a* -Diaza- *s* -Indacene (BODIPY) Dyads. *Organometallics* **2017**, *36* (18), 3435–3442. https://doi.org/10.1021/acs.organomet.7b00250.

(22) Gupta, G.; Kumari, P.; Ryu, J. Y.; Lee, J.; Mobin, S. M.; Lee, C. Y. Mitochondrial Localization of Highly Fluorescent and Photostable BODIPY-Based Ruthenium(II), Rhodium(III), and Iridium(III) Metal Complexes. *Inorg. Chem.* **2019**, *58* (13), 8587–8595. https://doi.org/10.1021/acs.inorgchem.9b00898.

(23) Bertrand, B.; Passador, K.; Goze, C.; Denat, F.; Bodio, E.; Salmain, M. Metal-Based BODIPY Derivatives as Multimodal Tools for Life Sciences. *Coord. Chem. Rev.* **2018**, *358*, 108–124. https://doi.org/10.1016/j.ccr.2017.12.007.

(24) Möltgen, S.; Piumatti, E.; Massafra, G.; Metzger, S.; Jaehde, U.; Kalayda, G. Cisplatin Protein Binding Partners and Their Relevance for Platinum Drug Sensitivity. *Cells* **2020**, *9* (6), 1322. https://doi.org/10.3390/cells9061322.

(25) Chu, G. M.; Fernández, I.; Guerrero-Martínez, A.; Ramírez de Arellano, C.; Sierra, M. A. Fluorescence Quenching in BODIPYs Having Ir- and Rh-Tethered Complexes. *Eur. J. Inorg. Chem.* **2016**, *2016* (6), 844–852. https://doi.org/10.1002/ejic.201501283.

(26) Miao, W.; Yu, C.; Hao, E.; Jiao, L. Functionalized BODIPYs as Fluorescent Molecular Rotors for Viscosity Detection. *Front. Chem.* **2019**, *7*, 825. https://doi.org/10.3389/fchem.2019.00825.

(27) Liu, X.; Chi, W.; Gómez-Infante, A. de J.; Peña-Cabrera, E.; Liu, X.; Chang, Y. A Systematic Study on the Relationship Between Viscosity Sensitivity and TEMPERATURE DEPENDENCY of BODIPY Rotors. *Bull. Korean Chem. Soc.* **2021**, *42* (1), 91–94. https://doi.org/10.1002/bkcs.12110.

(28) OECD. *Test No. 107: Partition Coefficient (n-Octanol/Water): Shake Flask Method*; 1995. https://doi.org/10.1787/9789264069626-en.

(29) Novohradsky, V.; Liu, Z.; Vojtiskova, M.; Sadler, P. J.; Brabec, V.; Kasparkova, J. Mechanism of Cellular Accumulation of an Iridium(III) Pentamethylcyclopentadienyl Anticancer Complex Containing a C,N-Chelating Ligand. *Metallomics* **2014**, *6* (3), 682–690. https://doi.org/10.1039/C3MT00341H.

(30) Murale, D. P.; Haque, M. M.; Hong, K. T.; Lee, J.-S. A Pyridinyl-Pyrazole BODIPY as Lipid Droplets Probe. *Bull. Korean Chem.*

Soc. **2021**, *42* (1), 111–114. https://doi.org/10.1002/bkcs.12166.

(31) Presley, A. D.; Fuller, K. M.; Arriaga, E. A. MitoTracker Green Labeling of Mitochondrial Proteins and Their Subsequent Analysis by Capillary Electrophoresis with Laser-Induced Fluorescence Detection. *J. Chromatogr. B* **2003**, *793* (1), 141–150. https://doi.org/10.1016/S1570-0232(03)00371-4.

(32) Nettebrock, N. T.; Bohnert, M. Born This Way – Biogenesis of Lipid Droplets from Specialized ER Subdomains. *Biochim. Biophys. Acta BBA - Mol. Cell Biol. Lipids* **2020**, *1865* (1), 158448. https://doi.org/10.1016/j.bbalip.2019.04.008.

(33) Conesa, J. J.; Carrasco, A. C.; Rodríguez-Fanjul, V.; Yang, Y.; Carrascosa, J. L.; Cloetens, P.; Pereiro, E.; Pizarro, A. M. Unambiguous Intracellular Localization and Quantification of a Potent Iridium Anticancer Compound by Correlative 3D Cryo X-Ray Imaging. *Angew. Chem. Int. Ed.* **2020**, *59* (3), 1270–1278. https://doi.org/10.1002/anie.201911510.

(34) Yang, Y.; Guo, L.; Tian, Z.; Gong, Y.; Zheng, H.; Zhang, S.; Xu, Z.; Ge, X.; Liu, Z. Novel and Versatile Imine-N-Heterocyclic Carbene Half-Sandwich Iridium(III) Complexes as Lysosome-Targeted Anticancer Agents. *Inorg. Chem.* **2018**, *57* (17), 11087–11098. https://doi.org/10.1021/acs.inorgchem.8b01656.

(35) Schulze, R. J.; Krueger, E. W.; Weller, S. G.; Johnson, K. M.; Casey, C. A.; Schott, M. B.; McNiven, M. A. Direct Lysosome-Based Autophagy of Lipid Droplets in Hepatocytes. *Proc. Natl. Acad. Sci.* **2020**, *117* (51), 32443–32452. https://doi.org/10.1073/pnas.2011442117.

(36) Olzmann, J. A.; Carvalho, P. Dynamics and Functions of Lipid Droplets. *Nat. Rev. Mol. Cell Biol.* **2019**, *20* (3), 137–155. https://doi.org/10.1038/s41580-018-0085-z.

(37) Petan, T.; Jarc, E.; Jusović, M. Lipid Droplets in Cancer: Guardians of Fat in a Stressful World. *Molecules* **2018**, *23* (8), 1941. https://doi.org/10.3390/molecules23081941.

(38) Shubin, A. V.; Demidyuk, I. V.; Komissarov, A. A.; Rafieva, L. M.; Kostrov, S. V. Cytoplasmic Vacuolization in Cell Death and Survival. *Oncotarget* **2016**, *7* (34), 55863–55889. https://doi.org/10.18632/oncotarget.10150.

(39) Huang, C.; Li, T.; Liang, J.; Huang, H.; Zhang, P.; Banerjee, S. Recent Advances in Endoplasmic Reticulum Targeting Metal Complexes. *Coord. Chem. Rev.* **2020**, *408*, 213178. https://doi.org/10.1016/j.ccr.2020.213178.

(40) Rozpedek, W.; Pytel, D.; Mucha, B.; Leszczynska, H.; Diehl, J. A.; Majsterek, I. The Role of the PERK/EIF2α/ATF4/CHOP Signaling Pathway in Tumor Progression During Endoplasmic Reticulum Stress. *Curr. Mol. Med.* **2016**, *16* (6), 533–544. https://doi.org/10.2174/1566524016666160523143937.

(41) Donnelly, N.; Gorman, A. M.; Gupta, S.; Samali, A. The EIF2α Kinases: Their Structures and Functions. 19.

(42) Tam, A. B.; Roberts, L. S.; Chandra, V.; Rivera, I. G.; Nomura, D. K.; Forbes, D. J.; Niwa, M. The UPR Activator ATF6 Responds to Proteotoxic and Lipotoxic Stress by Distinct Mechanisms. *Dev. Cell* **2018**, *46* (3), 327-343.e7. https://doi.org/10.1016/j.devcel.2018.04.023.

(43) Eisenberg-Lerner, A.; Benyair, R.; Hizkiahou, N.; Nudel, N.; Maor, R.; Kramer, M. P.; Shmueli, M. D.; Zigdon, I.; Cherniavsky Lev, M.; Ulman, A.; Sagiv, J. Y.; Dayan, M.; Dassa, B.; Rosenwald, M.; Shachar, I.; Li, J.; Wang, Y.; Dezorella, N.; Khan, S.; Porat, Z.; Shimoni, E.; Avinoam, O.; Merbl, Y. Golgi Organization Is Regulated by Proteasomal Degradation. *Nat. Commun.* **2020**, *11* (1), 409. https://doi.org/10.1038/s41467-019-14038-9.

(44) Oslowski, C. M.; Urano, F. Measuring ER Stress and the Unfolded Protein Response Using Mammalian Tissue Culture System. In *Methods in Enzymology*; Elsevier, 2011; Vol. 490, pp 71–92. https://doi.org/10.1016/B978-0-12-385114-7.00004-0.

(45) Qi, Y.; Liu, Z.; Li, H.; Sadler, P. J.; O'Connor, P. B. Mapping the Protein-Binding Sites for Novel Iridium(III) Anticancer Complexes Using Electron Capture Dissociation. *Rapid Commun. Mass Spectrom.* **2013**, *27* (17), 2028–2032. https://doi.org/10.1002/rcm.6643.

(46) Caterino, M.; Petruk, A. A.; Vergara, A.; Ferraro, G.; Marasco, D.; Doctorovich, F.; Estrin, D. A.; Merlino, A. Mapping the Protein-Binding Sites for Iridium(III)-Based CO-Releasing Molecules. *Dalton Trans.* **2016**, *45* (30), 12206–12214. https://doi.org/10.1039/C6DT01685E.

(47) Liu, Z.; Habtemariam, A.; Pizarro, A. M.; Clarkson, G. J.; Sadler, P. J. Organometallic Iridium(III) Cyclopentadienyl Anticancer Complexes Containing C,N-Chelating Ligands. *Organometallics* **2011**, *30* (17), 4702–4710. https://doi.org/10.1021/om2005468.

(48) Wang, B.; Liang, Y.; Dong, H.; Tan, T.; Zhan, B.; Cheng, J.; Lo, K. K.-W.; Lam, Y. W.; Cheng, S. H. A Luminescent Cyclometalated Iridium(III) Complex Accumulates in Mitochondria and Induces Mitochondrial Shortening by Conjugation to Specific Protein Targets. *ChemBioChem* **2012**, *13* (18), 2729–2737. https://doi.org/10.1002/cbic.201200517.

(49) King, A. P.; Wilson, J. J. Endoplasmic Reticulum Stress: An Arising Target for Metal-Based Anticancer Agents. *Chem. Soc. Rev.* **2020**, *49* (22), 8113–8136. https://doi.org/10.1039/D0CS00259C.

(50) Yue, Y.; Guo, Y.; Xu, J.; Shao, S. A Bodipy-Based Derivative for Selective Fluorescence Sensing of Homocysteine and Cysteine. *New J Chem* **2011**, *35* (1), 61–64. https://doi.org/10.1039/C0NJ00720J.

Table of Contents Graphic